

AlGaAs Tunnel Junction (TJ)-VCSELs: A NEGF-Drift-Diffusion Approach

Original

AlGaAs Tunnel Junction (TJ)-VCSELs: A NEGF-Drift-Diffusion Approach / Gullino, Alberto; Torrelli, Valerio; D'Alessandro, Martino; Tibaldi, Alberto; Bertazzi, Francesco; Goano, Michele; Debernardi, Pierluigi. - In: IEEE PHOTONICS JOURNAL. - ISSN 1943-0655. - ELETTRONICO. - 16:2(2024), pp. 1-9. [10.1109/jphot.2024.3360897]

Availability:

This version is available at: 11583/2986384 since: 2024-03-18T13:53:18Z

Publisher:

IEEE

Published

DOI:10.1109/jphot.2024.3360897


Terms of use:

This article is made available under terms and conditions as specified in the corresponding bibliographic description in the repository

Publisher copyright

(Article begins on next page)

AlGaAs Tunnel Junction (TJ)-VCSELs: A NEGF–Drift-Diffusion Approach

Alberto Gullino , *Member, IEEE*, Valerio Torrelli , Martino D'Alessandro , Alberto Tibaldi , *Member, IEEE*, Francesco Bertazzi , Michele Goano , *Senior Member, IEEE*, and Pierluigi Debernardi 

Abstract—This work reports a multiscale physics-based approach aimed at investigating the benefits of introducing a single tunnel junction (TJ) within conventional AlGaAs Vertical-Cavity Surface-Emitting Lasers (VCSELs). Our comprehensive VCSEL solver VENUS is augmented with a non-equilibrium Green's function (NEGF) approach to extract the band-to-band tunneling rate across the TJ. To showcase the NEGF-VENUS features, we apply it to the commercial *pin* oxide confined AlGaAs VCSEL previously investigated by VENUS, by inserting a TJ with minimal variations to the optical resonator. Besides finding the optimal position of TJ and oxide aperture, we can also compare the different hole injection schemes in the active region. Our results show the potential of doubling the maximum output power with the same threshold current, with perspectives of further enhancement by stacking more tunnel junctions.

Index Terms—Drift-diffusion, NEGF, physics-based, tunnel junction, VCSEL.

I. INTRODUCTION

NEAR-INFRARED Vertical-Cavity Surface-Emitting Lasers (VCSELs) based on AlGaAs represent the state-of-the-art of optical sources for short-reach optical interconnects in intradatacenter communication [1], [2], [3]. The benefits provided by VCSELs compared to edge-emitting lasers (EELs), including small beam divergence, low threshold current, high conversion efficiency and modulation speed [4], [5], are contributing to the startling VCSEL market expansion also in spectroscopic sensors [6] and atomic clocks [7]. Despite significant advancements in optimizing VCSELs for high-speed

optical communication, ensuring large output power, single transverse mode, and small-spot size for high-performance sensing remains a challenging endeavor.

Among other promising applications, a huge interest is drained by the 3D sensing to resemble the human sight. One particularly significant and demanding case pertains autonomously driving vehicles, whose LiDARs (Light Detection And Ranging) need uniform illumination at distances up to 100 m. LiDAR technology relies on time-of-flight methods employing pulsed VCSELs as light sources [8], [9], [10]. In this framework, an ideal light source necessitates single-mode output, narrow linewidth, and optical power larger than datacom applications. While enlarging the oxide aperture area is a common strategy to boost output power and detection range, this approach often introduces multiple transverse modes and a wider far-field divergence angle, detrimental sensitivity and precision [11], [12].

As first proposed by prof. Ebeling group [13], [14], [15], hole injection from a tunnel junction (TJ) enables an interesting solution to enhance the output power density keeping fixed the oxide aperture size. In that configuration, the internal quantum efficiency of the device is higher than one hundred percent by stacking more active stages. Carriers generating photons in each multi-quantum well (MQW) region are recycled by the TJs, i.e., the electrons recombined due to the stimulated emission recombination process, are re-promoted in the conduction band by the TJ and ready to restart the process [16], [17], [18].

In the recent years, TJs have been widely exploited in VCSELs to address issues related to confinement in aluminum free devices, such as in GaSb and InP-based VCSELs for 1.55–4 μm emission [19], [20], [21], and to overcome tricky technological processes needed to realize an effective acceptor doping in III-nitride VCSELs and LEDs for UV emission [22], [23].

TJs are reversely-biased heavily doped *pn* junctions where carrier transport is dominated by band-to-band tunneling (BTBT), requiring a proper quantum treatment [24]. For CAD purposes, a numerical VCSEL simulator should account for BTBT in TJ-VCSELs. In our previous work [25], we demonstrated the possibility of treating AlGaAs TJ-VCSELs within our in-house one dimensional drift-diffusion (DD) solver, by coupling it with a nonequilibrium Green's function (NEGF) approach [26], [27], [28], [29], [30]. In this work, the purpose is moving the NEGF-DD concept to our full VCSEL solver VENUS [31], [32], [33], capable of dealing with axisymmetric structures. To explore the potential of our NEGF-VENUS solver, we analyze two alternative designs of AlGaAs oxide-confined

Manuscript received 5 January 2024; revised 22 January 2024; accepted 25 January 2024. Date of publication 31 January 2024; date of current version 21 February 2024. This work was supported in part by the European Union under two initiatives of the Italian National Recovery and Resilience Plan (NRRP) of NextGenerationEU: the partnership on *Telecommunications of the Future* under Grant PE000000001 – Program RESTART, Project RIGOLETTO, and in part by the National Centre for HPC, Big Data and Quantum Computing under Grants CN000000013 – CUP and E13C22000990001. (Corresponding author: Alberto Gullino.)

Alberto Gullino and Pierluigi Debernardi are with the Consiglio Nazionale delle Ricerche (CNR), Istituto di Elettronica e di Ingegneria dell'Informazione e delle Telecomunicazioni (IEIIT), 10129 Turin, Italy (e-mail: alberto.gullino@polito.it).

Valerio Torrelli and Martino D'Alessandro are with the Department of Electronics and Telecommunications, Politecnico di Torino, 10129 Turin, Italy.

Alberto Tibaldi, Francesco Bertazzi, and Michele Goano are with the Consiglio Nazionale delle Ricerche (CNR), Istituto di Elettronica e di Ingegneria dell'Informazione e delle Telecomunicazioni (IEIIT), 10129 Turin, Italy, and also with the Department of Electronics and Telecommunications, Politecnico di Torino, 10129 Turin, Italy (e-mail: alberto.tibaldi@polito.it).

Digital Object Identifier 10.1109/JPHOT.2024.3360897

TJ-VCSELs, retrieved from a reference *pin* device where the carrier transport across the oppositely doped distributed Bragg's reflectors (DBRs) injects the electrons and holes inside the intrinsic cavity. By exploiting our physics-based multiphysics and multiscale approach, we extract the static electrical and optical characteristics of the three designs.

In Section II, the description of our electrical transport model is reported, with a focus on the modeling of the TJ characteristics based on NEGF formalism and its coupling with the DD model. In Section III, the reference *pin* VCSEL is described and, from this, two oxide-confined TJ-VCSELs are presented. Eventually, in Section IV, the results are compared and discussed to determine the best design. We also provide a subset of inner quantities, to help the discussion and grasp the reasons of different performances.

II. TJ-VCSEL MODELING

A comprehensive modeling of VCSELs needs to account for the electrical, optical and thermal problems, coupled self-consistently to determine the performance of these devices. Rate equation models are powerful tools to interpret experimental results on a wide set of semiconductor lasers, including VCSELs. However, they are not capable of predicting performance of new designs or extract the microscopic quantities of a device during its operation. VENUS has been developed by our group to attain this goal.

The purpose of this section is showing how the semiclassical carrier transport model based on a DD model has been extended to deal with the quantum tunneling across the TJ.

A. Drift-Diffusion Model for Bulk Transport

Carrier transport in conventional VCSELs can be assumed to occur within a local quasi-equilibrium condition, where a DD model can be employed. In VENUS, the DD model is solved numerically within a generalized Newton's scheme on a 2D spatial grid exploiting the cylindrical symmetry of the VCSELs under investigation. To ease the discussion, the model in its static version reported:

$$-\nabla^2 \phi = \frac{q}{\epsilon} (p - n + N_D^+ - N_A^-) \quad (1a)$$

$$\frac{1}{q} \nabla \cdot \mathbf{J}_n = R_{\text{rad}}^n + R_{\text{SRH}}^n + R_{\text{Aug}}^n + G_{\text{BTBT}} \quad (1b)$$

$$-\frac{1}{q} \nabla \cdot \mathbf{J}_p = R_{\text{rad}}^p + R_{\text{SRH}}^p + R_{\text{Aug}}^p + G_{\text{BTBT}}. \quad (1c)$$

The system (1) couples the Poisson (1a) with the carrier continuity (1b)–(1c). All the quantities involved are position-dependent. The unknowns of the system are the electrostatic potential ϕ and the electron and hole densities n and p . The elementary charge and dielectric constant are denoted by q and ϵ , respectively. In (1a), N_D^+ and N_A^- account for the ionized donor and acceptor doping densities [34], [35]. In (1b)–(1c), $R^{n/p}$ denote the rates accounting for radiative, Shockley-Read-Hall and Auger recombination.

In TJ-VCSELs, hole injection into the AR through the TJ is modeled as an additional generation mechanism G_{BTBT} , since

the non-local tunneling process can be formulated classically as electrons vanishing from the valence band on the p -side of the TJ and reappearing in the conduction band on the other side. This is further discussed in the next section.

The current densities \mathbf{J}_n and \mathbf{J}_p are extracted by the usual DD constitutive relations:

$$\mathbf{J}_n = -q\mu_n n \nabla \phi + qD_n \nabla n \quad (2a)$$

$$\mathbf{J}_p = -q\mu_p p \nabla \phi - qD_p \nabla p \quad (2b)$$

where $\mu_{n/p}$ and $D_{n/p}$ denote the electron and hole mobility and diffusivity, respectively, which are related by Einstein's relation.

In VENUS, the bulk DD model is extended with a set of quantum corrections to bridge electrical and optical models [36]. The QW optical response, that provides the gain and the spontaneous emission rate depending on carrier densities, temperature and output wavelength, is extracted by applying the Fermi's golden rule on an electronic band structure described with a 4-bands $\mathbf{k} \cdot \mathbf{p}$ method. Further details are discussed in depth in our previous work [33].

In this framework, the DD is applied to the whole structure. An example of energy band diagram obtained for a TJ-VCSEL at 3 V is reported in Fig. 1(a). In the indicated TJ region, conduction and valence band edges (E_C and E_V) are close enough to open a tunneling window (a zoom is provided in Fig. 1(b)), enabling a relevant tunneling current.

B. NEGF-DD Approach

The outlined model for the TJ-VCSEL simulations requires an accurate computation of the tunneling generation rate G_{BTBT} entering in (1b)–(1c). The BTBT models derived from Kane's work [37], such as the Hurkx's model that introduces a local tunneling recombination rate [38], [39], show some limitations when implemented in a DD approach [40], [41]. In *Sentaurus Device* by Synopsis [42], non-local tunneling models are available, describing real space transport across the TJ. Despite being more adherent to the physical phenomenon, the large amount of involved parameters affects their predictivity.

In this work, NEGF offers a pure quantum approach, capable of extracting the interband spectral current density J_{NEGF} [27], that is a position- and energy-resolved current across the TJ. This can be thought as the tunneling component of the current, with the intraband component modeled by the DD, resulting in a NEGF-DD scheme [25], [43].

The advantage of our approach comes from the calculation of the Green's functions limited to the TJ region, as reported in Fig. 1(b). In fact, the highly-doped layers impose the pinning of the quasi-Fermi levels, defining a well defined quantum region. The bands of the TJ computed with (1) serve as the Hartree potential for NEGF to solve the steady-state Keldysh and the Dyson equations within a finite element discretization of the space [44]. The nanostructure Hamiltonian derives from a multiband 8×8 $\mathbf{k} \cdot \mathbf{p}$ model of the electronic band structure including the first conduction band and heavy-hole, light-hole, and split-off valence bands to account for the tail states within the band gap of the material [45], [46]. The $\mathbf{k} \cdot \mathbf{p}$ parameters are taken from the semiempirical Luttinger coefficients in [47].

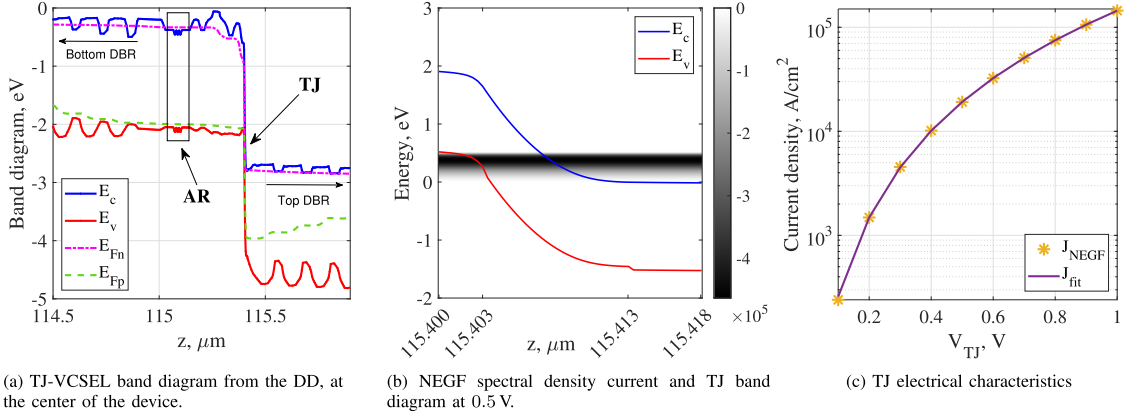


Fig. 1. (a) TJ-VCSEL energy band diagram at 3 V (red: VB, blue: CB) in the AR proximity, together with the quasi-Fermi levels (magenta: electrons; green: holes). The TJ position is indicated. (b) NEGF electron spectral current density (in black) as a function of position across the TJ, superimposed to the band diagram. The color bar expresses its magnitude in terms of $A/(eV \cdot cm^2)$. (c) TJ characteristics from NEGF (yellow stars) and corresponding power fit (purple line).

The low aluminum fraction of the involved AlGaAs TJ yields a direct band gap in the symmetric Γ -valley, so that phonon-assisted tunneling connecting valleys with different wave vectors does not play a significant role [48], [49], [50]. In [25], a comparison between the electrical characteristics obtained from fully scattered Green's functions and coherent limit demonstrates that a ballistic assumption is acceptable for the investigated TJ.

Although the computational effort is reduced by employing the ballistic assumption, NEGF is not executed in the DD scheme to prevent prolonged simulations. Instead, NEGF simulations are conducted in across a voltage range from 0 to 1 V, in order to extract J_{NEGF} . In Fig. 1(b), J_{NEGF} is superimposed to the TJ band diagram at 0.5 V. The negative values of J_{NEGF} correspond to positive carrier velocity, therefore injecting holes at the p -side. Then, J_{NEGF} is integrated in energy (as it is position independent, following the ballistic assumption), and the resulting current density J_{TJ} is reported as yellow stars in Fig. 1(c).

The successive coupling between NEGF and DD is realized by computing a proper G_{BTBT} , starting from J_{TJ} . The TJ voltage drop V_{TJ} is introduced:

$$V_{TJ} = E_{F_p}(p\text{-side}) - E_{F_n}(n\text{-side}) \quad (3)$$

where E_{F_p} and E_{F_n} denote the quasi-Fermi levels (green and magenta curves in Fig. 1(a)), computed within the DD simulation. Then, J_{TJ} is fitted by a power fit:

$$J_{TJ}(V_{TJ}) = 10^\alpha A/cm^2, \quad \text{where } \alpha = \sum_{i=0}^{10} \beta_i V_{TJ}^i \quad (4)$$

with β_i being the fit coefficients. The purple line in Fig. 1(c) is obtained from (4), superimposed to the integrated NEGF spectral current. The storage of $J_{TJ}(V_{TJ})$ in a look-up table avoids to run heavy NEGF simulations at every DD iteration. V_{TJ} extrapolates J_{TJ} using (4), and it is finally plugged in:

$$G_{BTBT}(z, V_{TJ}) = \begin{cases} \frac{1}{q} \frac{J_{TJ}(V_{TJ})}{L_{TJ}}, & \text{if } z \in \text{TJ} \\ 0, & \text{elsewhere} \end{cases} \quad (5)$$

to retrieve a uniform BTBT generation term G_{BTBT} in the TJ region, with $L_{TJ} = 18$ nm TJ thickness. $G_{BTBT}(V_{TJ})$ is inserted in (1b)–(1c), to bridge NEGF and DD in VENUS.

A similar procedure was validated in [25], where experimental data on a test structure designed and characterized by Chalmers University have been reproduced by our NEGF-DD approach, within a one-dimensional electrical solver.

III. INVESTIGATED STRUCTURES

The AlGaAs *pin* VCSEL investigated in [32] serves as a reference device. It is a commercial VCSEL emitting at 850 nm, with measurements provided by Ulm University. It features a 1λ -optical cavity embedding three 8 nm GaAs QWs. The top out-coupling DBR is made of 21 pairs of p -doped $Al_{0.17-0.90}GaAs$ layers, with N_A varying between $7 \cdot 10^{18}$ and $3 \cdot 10^{19} cm^{-3}$. The 36 pairs of the bottom DBR are n -doped with N_D from 2 to $9 \cdot 10^{18} cm^{-3}$. The oxide aperture, for optical and electrical confinement, has a diameter of $4.35 \mu m$ and provides both current and optical confinements. It is 30 nm thick to keep at minimum the scattering losses [51], [52]. After thinning, the structure lies on a $110 \mu m$ thick n -type GaAs substrate. The top metallic contact consists of a metal ring (inner radius $6 \mu m$) deposited on the topmost GaAs layer, where an ohmic contact is realized with a heavily p -doped GaAs layer with thickness 140 nm. After the metallic contact definition, the GaAs layer is etched down by 60 nm in the inner section of the metal ring.

The p -doping in the top DBR limits the *pin* VCSELS performance, as it worsens free-carrier absorption (FCA) losses and electrical conductivity inducing an earlier thermal rollover that limits the peak optical power. In this work, the TJ is used to convert the top DBR doping into n -type. To prove the potential of NEGF-VENUS, two oxide-confined TJ-VCSEL configurations are analyzed.

A. Oxide-Confined TJ-VCSEL Design

The impact of the reciprocal position of oxide and TJ on confinement is addressed by maintaining the designs as close as possible to the reference *pin* device. This allows a direct

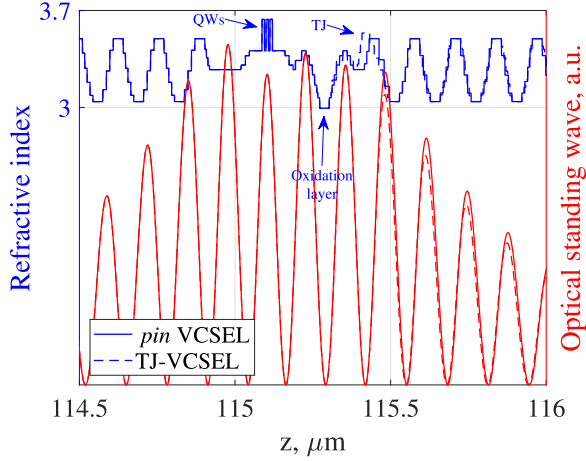


Fig. 2. Blue: refractive index profile $n_r(z)$ of *pin* (solid line) and TJ-VCSELs (dashed line). The output facet is at right of the QWs. $n_r(z)$ are superimposed, unless for the TJ ($z \approx 115.3 \mu\text{m}$). Red: optical standing waves.

comparison of the two hole injection schemes (from *p*-DBR or from TJ). The refractive index profiles n_r of *pin* and one of the two TJ-VCSEL configurations are reported as blue lines in Fig. 2, showing a difference in the TJ region.

An immediate advantage is the technological compatibility with the standard VCSEL growing techniques. The relevant differences are the dopant species (Te instead of Si) needed to attain high doping levels ($N_D = 3 \cdot 10^{19} \text{ cm}^{-3}$) in the TJ *n*-side [53], [54], [55] and the top DBR *n*-doping, equal to the bottom one. The TJ *p*-side is C-doped, with density $N_A = 2 \cdot 10^{20} \text{ cm}^{-3}$.

The low Te diffusion allows to assume an abrupt doping profile across the TJ [56]. From this assumption, an absorption $\alpha_{\text{TJ}} \approx 2500 \text{ cm}^{-1}$ is computed for the TJ using the formula reported in [57, p. 175]:

$$\alpha = f_\alpha \left(\alpha_n \frac{n}{10^{18} \text{ cm}^{-3}} + \alpha_p \frac{p}{10^{18} \text{ cm}^{-3}} \right) \quad (6)$$

with coefficients $\alpha_{n,p}$ and fitting factor f_α extracted in [32] and equal to 3, 7 and 2.9 respectively. From (6), the longitudinal absorption coefficients are extracted for *pin* and a TJ-VCSEL, and reported in Fig. 3. The purple line refers to the TJ-VCSEL, showing the aforementioned strong absorption peak in the TJ ($z \approx 115.3 \mu\text{m}$). The yellow curve refers to the *pin* VCSEL. In the bottom DBR, that extends on the left before $115 \mu\text{m}$, α_{pin} is superimposed to the TJ-VCSEL profile, as the devices are identical. At the outcoupling side, the top DBR begins at $\approx 115.4 \mu\text{m}$ and the TJ-VCSEL displays a relevant absorption coefficient reduction, dropping from $40\text{--}60 \text{ cm}^{-1}$ of the *p*-DBR to $5\text{--}20 \text{ cm}^{-1}$ of the *n*-DBR, identical to the bottom DBR. Between 115 and $115.1 \mu\text{m}$, very similar α values are predicted by our model for the ARs.

The benefit of introducing a TJ within a conventional *pin* VCSEL is the switch of the outcoupling mirror doping type. The consequent reduction of the FCA in *n*-doped materials allows to reduce by two the number of top DBR pairs. As a result, our optical solver VELM [58], [59], [60] predicts a matched threshold gain G_{th} for the two structures, namely,

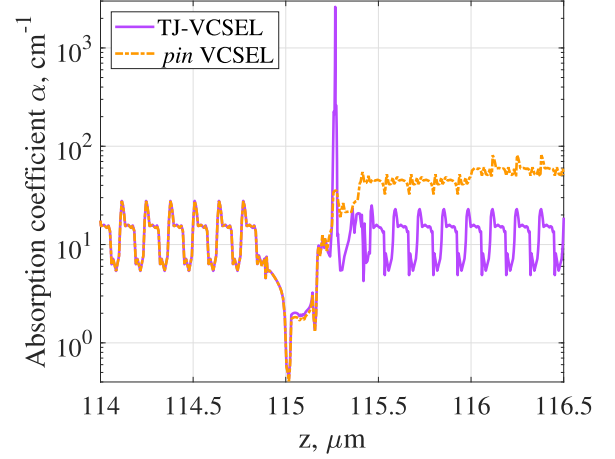


Fig. 3. Longitudinal absorption coefficient profiles $\alpha(z)$ of *pin* and TJ-VCSELs. In the TJ-VCSEL (purple line) there is a peak in the TJ, whereas in the top DBR (right mirror) it is greatly reduced compared to *pin* device (orange dashed line). In the bottom DBR, α are superimposed.

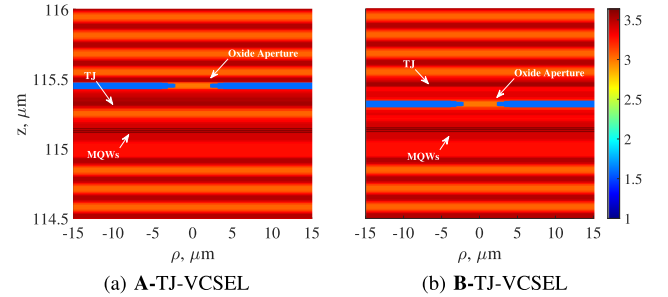


Fig. 4. Refractive index profiles of the TJ-VCSELs, in the AR proximity. The oxide aperture is surrounded by the oxidized region (light blue). Oxide aperture and TJ position is switched, to place both elements in the SW nodes.

$G_{\text{th}} = 1440 \text{ cm}^{-1}$ for the *pin* VCSEL, and $G_{\text{th}} = 1480 \text{ cm}^{-1}$ for the TJ-VCSELs.

B. TJ and Oxide Aperture Placement

Great attention must be devoted to the position of the oxide aperture. In fact, if inserted in a node of the optical standing wave (SW) in the outcoupling DBR and in the AR proximity, it guarantees weak transverse mode guiding [61], [62]. Similarly, the TJ should be placed in a SW node above the AR, to reduce its strong impact on the FCA. The position of both elements can be appreciated from the SW reported as red curves in Fig. 2.

In Fig. 4, the TJ-VCSELs are sketched in terms of two-dimensional refractive index profiles. Substrate and DBRs (represented in shades of orange and red) are not shown in full, as they are identical. The radially graded oxide aperture is surrounded by the oxidized region (light blue); three dark stripes in the AR denote the QWs; the TJ has an Al molar fraction close to the DBR, and is indicated in the figure. The relevant difference lies in the reciprocal position of oxide aperture and TJ, keeping fixed their 1λ distance. When the oxide aperture is placed above the TJ, the latter lies in the first node and the oxide is grown in the very next one (see Fig. 4(a)), hereinafter referred

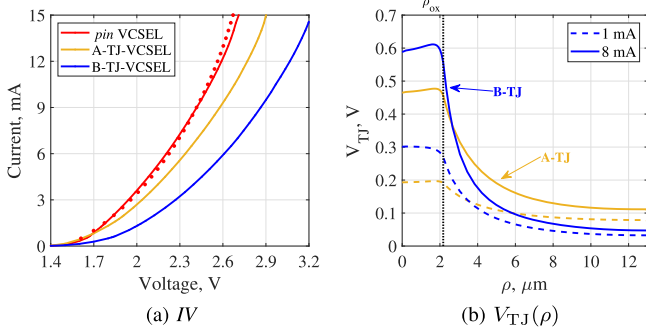


Fig. 5. (a): static electrical characteristics (*IV*) and (b) TJ voltage drop V_{TJ} as a function of radius ρ , at two bias currents. Yellow: A-TJ; blue: B-TJ-VCSEL. Dashed lines: 1 mA; solid lines: 8 mA.

to as A-TJ-VCSEL. Conversely, in case of oxide aperture below the TJ (between the latter and the AR), the position of the two elements is switched (see Fig. 4(b)), hereinafter referred to as B-TJ-VCSEL.

IV. RESULTS

This section will focus on macroscopic and microscopic VENUS quantities to compare the reference *pin* and the proposed TJ-VCSELS. The comparison between static electrical and optical characteristics at room temperature is supported by an analysis of the confinement in the structures, to get insights about a proper placement of the TJ.

A. Electrical Characteristics

To determine the impact of introducing a TJ, the section begins with a comparison of the current-voltage *IV* characteristics, as presented in Fig. 5(a).

The results for the *pin* device computed by VENUS (red solid line) are in good accordance with the experimental data, marked with dots [32]. Moving the focus on the TJ-VCSELS – yellow line: A-TJ; blue line: B-TJ-VCSEL – the *IV* curves are affected by the TJ. In fact, the exponential characteristics reported in Fig. 1(c) makes the TJ working as a diode in series with the *pin* junction. In this view, the TJ enables a significant current flow inside the TJ-VCSEL when V_{TJ} sustains a relevant BTBT current. At equal bias current is applied to the three devices, the overall voltage drop is larger in the A-TJ-VCSEL, and even more in the B-TJ-VCSEL, compared to the reference device. Our physics-based in-house solver allows to go deep into the details of each device operation, to explain such an electrical penalty.

In Fig. 5(b), V_{TJ} computed according to (3) is reported as a function of VCSEL radius ρ , at two bias points (1 and 8 mA) for both the TJ-VCSELS. In the A-TJ-VCSEL, V_{TJ} is lower for $\rho < \rho_{ox}$: according to (4), B-TJ-VCSEL sustains a stronger tunneling current within the confined region. Conversely, V_{TJ} decreases less steeply for $\rho_{ox} < \rho < \rho_{mesa}$, yielding a greater tunneling current that worsens the confinement.

To understand the reasons leading to different V_{TJ} , and thus the *IV*, we report the arrow plots of Fig. 6, superimposed to the 2D VCSEL scheme, at 8 mA. The colored blocks highlight AR

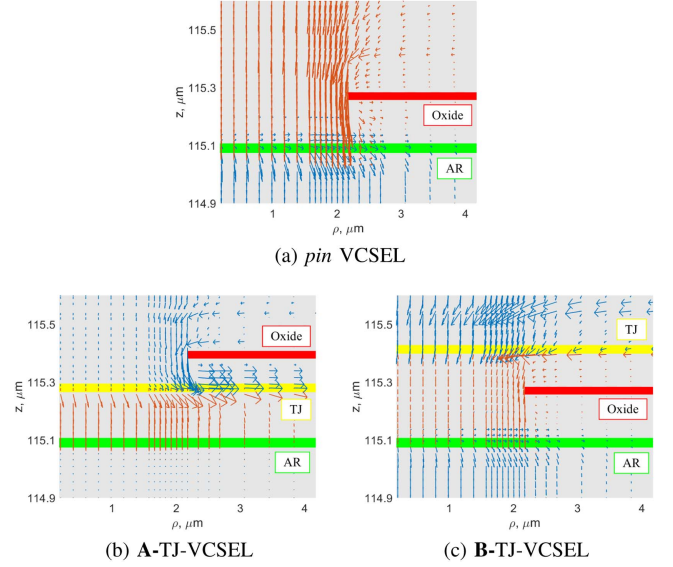


Fig. 6. Arrow plots of electron (blue) and hole (orange) current densities, in (a) *pin*, (b) A-TJ- and (c) B-TJ-VCSEL, at bias current 8 mA. Green regions: AR; yellow: TJ; red: oxide.

(green), oxide (red) and TJ (yellow). The normalized length of arrows is proportional to the current intensity in that mesh point (blue: J_n ; orange: J_p).

As expected, in the *pin* VCSEL (Fig. 6(a)), *p*-current dominates the overall current density above the oxide and the AR, as injection is demanded to hole transport across the *p*-DBR. On the other hand, the TJ injects holes into the cavity through tunneling: when the oxide is placed below the TJ (Fig. 6(c)), the VCSEL has a configuration similar to its *pin* counterpart. Electrons from the top contact reach the planar TJ and are “converted” into holes, that undergo the current crowding effect. As a consequence, the electrical penalty in the *IV* is almost equal to the voltage drop across the TJ itself. The confinement is effective, as the lower mobility of holes prevent their spreading before reaching the AR. When oxide and TJ position is switched in the A-TJ-VCSEL (Fig. 6(b)), the aperture confines J_n (see the blue arrows pointing toward left). Then, electrons reach the TJ, where the strong doping level induces a relevant diffusion current that makes the blue arrows change their orientation. Current spreading increases below the oxide, counteracting the electrical confinement, and thus reducing the voltage penalty of the device.

B. Optical Characteristics

As demonstrated, the designs yield different electrical confinement features. To assess the impact of a modified confinement, in Fig. 7 (top) the output optical power is reported as a function of current (*LI*). The LP notation is used to denote the modes, whose shape is reported at the bottom of Fig. 7: LP₀₁ for the Gaussian-like mode; LP₀₂ for the second radial mode with no azimuthal variations; LP₁₁ for the first-order mode. They are denoted as \circ , $*$ and ∇ , respectively.

VENUS predicts a threshold current $I_{th} \approx 500 \mu\text{A}$ for the reference VCSEL (in red). Fundamental LP₀₁ mode is the first

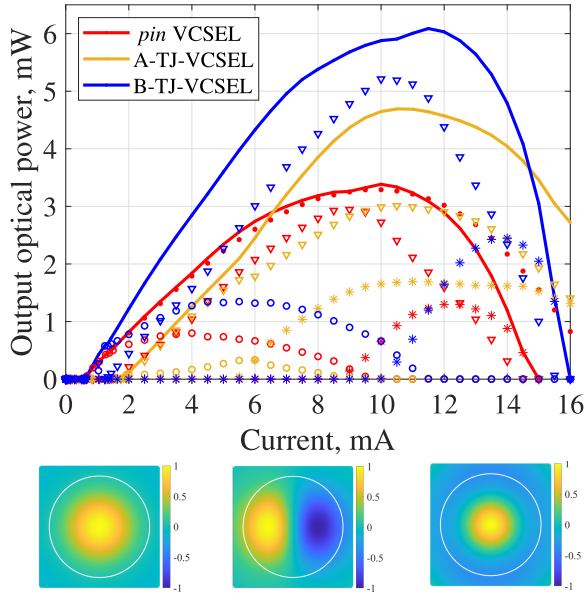


Fig. 7. Top: Output optical power as a function of current (LI), for the three VCSELs under analysis. Bottom: investigated modes. From left to right: LP_{01} (\circ), Gaussian-like mode; LP_{11} (∇), first order mode; LP_{02} ($*$), second radial mode. The white circles denote the oxide aperture.

to reach lasing condition due to negligible thermal guiding and spatial hole burning (SHB). At 2 mA, the internal self-heating is still not relevant, but LP_{11} turns on due to the SHB and becomes dominant at 4 mA. Entering the roll-over condition, LP_{02} starts lasing at 9 mA and reaches its peak at 12 mA. Such modal separation is ensured by the oxide position, in the first SW node after the AR [61], [62]. The overall output optical power is in good accordance with experimental result (red dots). The maximum total output power $P_{\max} = 3.3$ mW is reached at a bias current $I \approx 10$ mA.

Similar considerations apply to the B-TJ-VCSEL LI curve, in blue. Oxide confinement is introduced in a similar position than in the pin VCSEL, inducing a comparable modal separation, with similar threshold currents for all the modes. The thinner outcoupling mirror enhances the optical slope dL/dI of the emitted modes, almost doubling P_{\max} (6 mW) at a similar current of the pin device.

In pin and B-TJ-VCSELs, I_{th} is related to the LP_{01} threshold. For the A-TJ-VCSEL, $I_{th} \approx 1.7$ mA refers to LP_{11} (yellow ∇). The poor electrical confinement affects the carrier distribution inside the QWs and the gain shape (see discussion in the next paragraph), hindering the fundamental mode emission. Consequently, the gain-field product of LP_{11} favors it against LP_{01} , that delivers a power lower than 0.5 mW. At 5.5 mA, LP_{02} reaches its threshold, diminished from 10 mA of the B-TJ-VCSEL. Even though it never becomes dominant, it increases the overall dL/dI and provides a robust contribution to the LI , also beyond roll-over, suggesting that thermal guiding favors LP_{02} for a wide current range. Due to the same mirror losses, the total dL/dI slope remains similar to the B-TJ-VCSEL, but P_{\max} is reduced to 4.7 mW at 10.5 mA. The assessment of the optical characteristics indicates that the oxide aperture should not be placed above the TJ.

The reasons of a different optical behavior are strictly related to the previously discussed electrical properties. SHB governs the modal competition, as a lower hole mobility determines the radial gain profile inside the QWs. The role of SHB and thermal effects as fundamental mechanisms selecting the dominant lasing mode is discussed starting from Fig. 8, a set of VENUS inner quantities taken in the central QW.

The radial shape of the considered modes intensity is displayed in Fig. 8(a). The interaction of the optical fields with the carrier reservoir causes a local depletion induced by stimulated recombination. The radial distribution of the carriers in the QW at 1 and 10 mA is displayed in Fig. 8(b).

At 1 mA, pin and B-TJ-VCSELs QW filling is similar, dropping after ρ_{ox} ; in the A-TJ-VCSEL, only halved values are reached. Electrons (solid lines) and holes (squares) are superimposed. The corresponding gain profile (continuous lines in Fig. 8(c)) depends on carrier densities and temperature. For the A-TJ-VCSEL, gain is negative, meaning that the QWs are still in the absorbing region. This reflects in the already discussed static LI curves: at 1 mA, the A-TJ-VCSEL has not reached the optical threshold yet, while pin and B-TJ-VCSELs are already lasing. At 10 mA, electrons (dashed lines) and holes (diamonds) of pin and B-TJ-VCSELs split due to the SHB (Fig. 8(b)). Gain profile changes, favoring the emission of higher order modes (dashed lines in Fig. 8(c)). In the A-TJ-VCSEL, carriers density remains high also outside ρ_{ox} . This indicates poor confinement and explains the delayed threshold and the reduced modal powers.

C. Efficiency and Output Emission Wavelength

As discussed, the B-TJ-VCSEL features an almost doubled maximum output power compared to the pin device, as the LI slope is enhanced due the top DBR doping conversion. However, the electrical characteristics highlights a penalty due to the presence of the TJ. In Fig. 9, the wall-plug efficiency (η_{WP}) curves demonstrate the overall enhancement resulting from the TJ hole injection scheme and the top DBR doping conversion. For the B-TJ-VCSEL the maximum η_{WP} rises from $\approx 23\%$ (pin) to $\approx 31\%$. In the whole operation range, pin efficiency lies below the B-TJ-VCSEL. Furthermore, a number of applications prioritize output power density and efficiency over higher bias voltage [10]. In contrast, η_{WP} in the A-TJ-VCSEL increases less steeply, after the delayed threshold, and outperforms pin VCSEL efficiency at 7 mA. No improvement comes from A-TJ-VCSEL compared to the alternative design.

The static characteristics analysis is closed by the comparison of the emission wavelength λ , as a function of the bias current, reported in Fig. 10. This figure of merit represents the easiest way to determine the inner temperature rise during VCSELs operation, due to the wavelength red-shift phenomenon. At low bias currents (close to the cold cavity condition), λ of the three investigated devices is similar (~ 848 nm). The $\lambda(I)$ curve for the pin VCSEL well reproduces the experimental data (open circles), for currents larger than 6 mA. The thermal shift with temperature remains below 0.05 nm/K. Top DBR doping conversion limits the self-heating induced by FCA in the

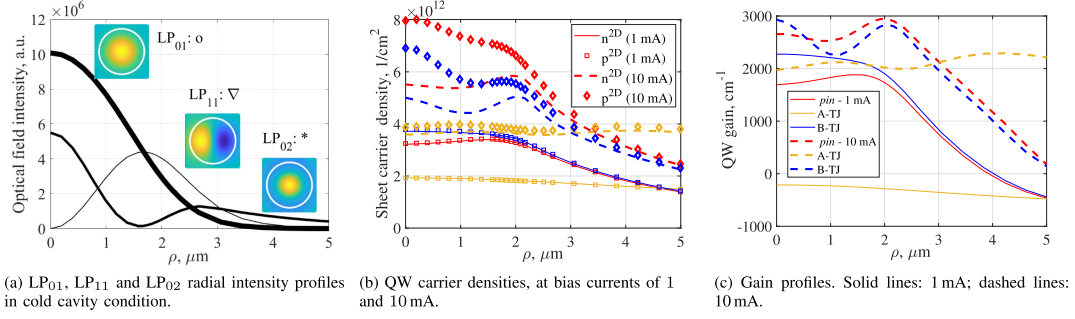


Fig. 8. Radial quantities extracted in the central QW. (a) Modal intensities extracted by VELM. (b) QW sheet electron and hole densities at bias currents of 1 and 10 mA (see legend for the symbols meaning). (c) Gain profiles computed employing the Fermi's golden rule at the same current values. In (b)–(c), red, yellow and blue curves refer to pin , A-TJ and B-TJ-VCSELS, respectively.

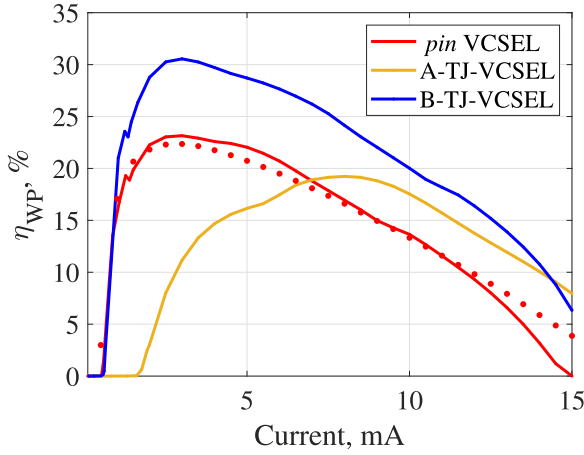


Fig. 9. Wall-plug efficiency as a function of bias current of the VCSELs under investigation. Red dots: experimental data on the pin VCSEL. Continuous lines: VENUS results.

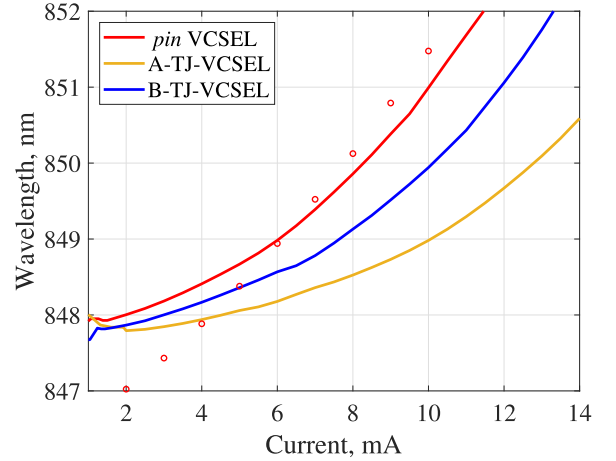


Fig. 10. Emission wavelength as a function of bias current of the VCSELs under investigation. Red circles: experimental data on the pin VCSEL. Continuous lines: VENUS results.

TJ-VCSELS. They show improved thermal stability, as proven by the smaller λ at equal bias currents. The difference between A- and B-TJ-VCSEL is related to smaller optical powers reached by the first, that further limits self-heating.

V. CONCLUSION

The demand of VCSELS for large distance 3D sensing requires solutions to reach higher output powers. A convenient path involves the modification of widespread AlGaAs VCSELS by introducing a TJ inside their structures, to enhance their performance.

Having validated our NEGF-DD in a 1D electrical solver [25], we present for the first time the results of our NEGF-DD approach applied in VENUS, allowing full physics-based TJ-VCSEL simulations. We extract from NEGF the TJ electrical characteristics, used to compute a BTBT generation rate that couples NEGF with the DD model.

To showcase the capabilities of the augmented VENUS, two test oxide-confined TJ-VCSELS are investigated. Starting from a conventional pin VCSEL, a comparison of the static characteristics shows that the oxide in a TJ-VCSEL must be

placed in the node closest to the AR, with the TJ above it. This mimics the pin operation: despite higher voltages, the threshold current remains equal, and the maximum output power is doubled.

The presented results are the initial steps towards more complex structures involving TJs, including the multijunction VCSELS. VENUS could be a powerful tool to determine the proper positioning of the oxide apertures between each stacked AR. An even more interesting design could involve the photolithographic definition of buried TJs, to get rid of the wet oxidation process that limits the effectiveness of confinement when going to small oxide diameters [63], [64]. At the same time, the definition of a mesa would not be necessary any more, resulting in denser VCSEL arrays [65], [66].

REFERENCES

- [1] J. A. Tatum et al., "VCSEL-based interconnects for current and future data centers," *J. Lightw. Technol.*, vol. 33, no. 4, pp. 727–732, Feb. 2015.
- [2] N. Ledentsov Jr., M. Agustin, L. Chorchos, N. N. Ledentsov, and J. P. Turkiewicz, "25.78 gbit/s data transmission over 2 km multi-mode-fibre with 850 and 910 nm single-mode VCSELS and a commercial quad small form-factor pluggable transceiver," *Electron. Lett.*, vol. 54, no. 12, pp. 774–775, 2018.

- [3] A. Larsson, J. S. Gustavsson, A. Fölöp, E. Haglund, E. P. Haglund, and A. Kelkkanen, "The future of VCSELs: Dynamics and speed limitations," in *Proc. IEEE Photon. Conf.*, 2020, pp. 1–2.
- [4] A. Liu, P. Wolf, J. A. Lott, and D. Bimberg, "Vertical-cavity surface-emitting lasers for data communication and sensing," *Photon. Res.*, vol. 7, no. 2, pp. 121–136, 2019.
- [5] N. N. Ledentsov et al., "High speed VCSEL technology and applications," *J. Lightw. Technol.*, vol. 40, no. 6, pp. 1749–1763, Mar. 2022.
- [6] G. K. Veerabathran, S. Sprengel, A. Andrejew, and M.-C. Amann, "Room-temperature vertical-cavity surface-emitting lasers at 4 μm with GaSb-based type-II quantum wells," *Appl. Phys. Lett.*, vol. 110, 2017, Art. no. 071104.
- [7] M. Huang, D. K. Serkland, and J. Camparo, "A narrow-linewidth three-mirror VCSEL for atomic devices," *Appl. Phys. Lett.*, vol. 121, no. 11, Sep. 2022, Art. no. 114002.
- [8] H. Moench et al., "VCSEL-based sensors for distance and velocity," in *Proc. SPIE*, vol. 976, 2016, Art. no. 97660A, doi: [10.1117/12.2209320](https://doi.org/10.1117/12.2209320).
- [9] I. Kim et al., "Nanophotonics for light detection and ranging technology," *Nature Nanotechnol.*, vol. 16, no. 5, pp. 508–524, 2021.
- [10] M. M. Dummer, A. Ghods, G. Xu, S. Rothwell, and K. Johnson, "Single-mode multi-junction VCSELs with integrated transverse mode filter," in *Proc. SPIE*, vol. 12439, pp. 58–65, 2023.
- [11] H. Liu, P. Miao, Y. Xiao, C. Liu, Z. Zhang, and J. Wang, "High performance multi-junction VCSELs for LiDAR applications," in *Proc. SPIE*, vol. 12020, pp. 15–22, 2022.
- [12] Y. Li et al., "High-gain InAlGaAs quaternary quantum wells for high-power 760 nm two-junction VCSELs," *IEEE J. Quantum Electron.*, vol. 59, no. 5, Oct. 2023, Art. no. 2400508.
- [13] T. Knödl et al., "CW room temperature operation of a diode cascade InGaAs-AlGaAs quantum well VCSEL," in *Proc. IEEE LEOS Annu. Meeting Conf. Proc. 12th Annu. Meeting. IEEE Lasers Electro- Opt. Soc. Annu. Meeting*, 1999, pp. 143–144.
- [14] T. Knödl, M. Golling, A. Straub, and K. J. Ebeling, "Multi-diode cascade VCSEL with 130% differential quantum efficiency at CW room temperature operation," *Electron. Lett.*, vol. 37, pp. 31–33, Jan. 2001.
- [15] T. Knödl, M. Golling, A. Straub, R. Jager, R. Michalzick, and K. Ebeling, "Multistage bipolar cascade vertical-cavity surface-emitting lasers: Theory and experiment," *IEEE J. Select. Topics Quantum Electron.*, vol. 9, no. 5, pp. 1406–1414, Sep./Oct. 2003.
- [16] G. Pan, M. Xun, Z. Zhao, Y. Sun, J. Zhou, and D. Wu, "High slope efficiency bipolar cascade 905 nm vertical-cavity surface-emitting laser," *IEEE Electron Device Lett.*, vol. 42, no. 9, pp. 1342–1345, Sep. 2021.
- [17] Y. Zhao et al., "Epitaxially-stacked high efficiency laser diodes near 905 nm," *IEEE Photon. J.*, vol. 14, no. 6, pp. 1–6, Dec. 2022.
- [18] H. Wenzel, A. Maaßdorf, C. Zink, D. Martin, M. Weyers, and A. Knigge, "Novel 900 nm diode lasers with epitaxially stacked multiple active regions and tunnel junctions," *Electron. Lett.*, vol. 57, no. 11, pp. 445–447, 2021.
- [19] W. Hofmann, M. Muller, G. Böhm, M. Ortsiefer, and M.-C. Amann, "1.55- μm VCSEL with enhanced modulation bandwidth and temperature range," *IEEE Photon. Technol. Lett.*, vol. 21, no. 13, pp. 923–925, Jul. 2009.
- [20] A. Bachmann, K. Kashani-Shirazi, S. Arafin, and M.-C. Amann, "GaSb-based VCSEL with buried tunnel junction for emission around 2.3 μm ," *IEEE J. Select. Topics Quantum Electron.*, vol. 15, pp. 933–940, 2009.
- [21] A. Andrejew, S. Sprengel, and M.-C. Amann, "GaSb-based vertical-cavity surface-emitting lasers with an emission wavelength at 3 μm ," *Opt. Lett.*, vol. 41, no. 12, pp. 2799–2802, 2016.
- [22] J. T. Leonard et al., "Demonstration of a III-nitride vertical-cavity surface-emitting laser with a III-nitride tunnel junction intracavity contact," *Appl. Phys. Lett.*, vol. 107, no. 9, 2015, Art. no. 091105.
- [23] Y. Zhang, Z. Jamal-Eddine, and S. Rajan, "Recent progress of tunnel junction-based ultra-violet light emitting diodes," *Japan. J. Appl. Phys.*, vol. 58, May 2019, Art. no. SC0805.
- [24] L. Esaki, "New phenomenon in narrow germanium p - n junctions," *Phys. Rev.*, vol. 109, no. 2, pp. 603–604, Jan. 1958.
- [25] A. Tibaldi et al., "Analysis of carrier transport in tunnel-junction vertical-cavity surface-emitting lasers by a coupled nonequilibrium Green's function–drift-diffusion approach," *Phys. Rev. Appl.*, vol. 14, no. 2, Aug. 2020, Art. no. 024037.
- [26] T. A. Ameen, H. Ilatikhameneh, J. Z. Huang, M. Povolotskiy, R. Rahman, and G. Klimeck, "Combination of equilibrium and nonequilibrium carrier statistics into an atomistic quantum transport model for tunneling heterojunctions," *IEEE Trans. Electron Devices*, vol. 64, no. 6, pp. 2512–2518, Jun. 2017.
- [27] F. Bertazzi, A. Tibaldi, M. Goano, J. A. G. Montoya, and E. Bellotti, "Nonequilibrium green's function modeling of type-II superlattice detectors and its connection to semiclassical approaches," *Phys. Rev. Appl.*, vol. 14, no. 1, Jul. 2020, Art. no. 014083.
- [28] A. Tibaldi, J. A. G. Montoya, M. Vallone, M. Goano, E. Bellotti, and F. Bertazzi, "Modeling infrared superlattice photodetectors: From nonequilibrium green's functions to quantum-corrected drift diffusion," *Phys. Rev. Appl.*, vol. 16, no. 4, Oct. 2021, Art. no. 044024.
- [29] Y. Yin, C. Shao, H. Guo, J. Robertson, Z. Zhang, and Y. Guo, "Negative differential resistance effect in "cold" metal heterostructure diodes," *IEEE Electron Device Lett.*, vol. 43, no. 3, pp. 498–501, Mar. 2022.
- [30] H. Guo et al., "Quantum transport of sub-5 nm InSe and In₂SSe monolayers and their heterostructure transistors," *Nanoscale*, vol. 15, pp. 3496–3503, 2023. [Online]. Available: <http://dx.doi.org/10.1039/D2NR07180K>
- [31] A. Tibaldi, F. Bertazzi, M. Goano, R. Michalzick, and P. Debernardi, "VENUS: A vertical-cavity surface-emitting laser electro-opto-thermal NUmberical simulator," *IEEE J. Select. Topics Quantum Electron.*, vol. 25, no. 6, Nov./Dec. 2019, Art. no. 1500212.
- [32] P. Debernardi, A. Tibaldi, M. Daubenschütz, R. Michalzick, M. Goano, and F. Bertazzi, "Probing thermal effects in VCSELs by experiment-driven multiphysics modeling," *IEEE J. Select. Topics Quantum Electron.*, vol. 25, no. 6, Nov./Dec. 2019, Art. no. 1700914.
- [33] A. Tibaldi et al., "Bridging scales in multiphysics VCSEL modeling," *Opt. Quantum Electron.*, vol. 51, no. 7, Jul. 2019, Art. no. 231.
- [34] M. Lades, W. Kaindl, N. Kaminski, E. Niemann, and G. Wachutka, "Dynamics and incomplete ionized dopants and their impact on 4H/6H–SiC devices," *IEEE Trans. Electron Devices*, vol. 46, no. 3, pp. 598–604, Mar. 1999.
- [35] R. Heilman and G. Oelgart, "Ionization energy of the carbon acceptor in Al_xGa_{1-x}As," *Semicond. Sci. Technol.*, vol. 5, pp. 1040–1045, 1990.
- [36] M. Grupen and K. Hess, "Simulation of carrier transport and nonlinearities in quantum-well laser diodes," *IEEE J. Quantum Electron.*, vol. 34, no. 1, pp. 120–140, Jan. 1998.
- [37] E. Kane, "Zener tunneling in semiconductors," *J. Phys. Conf. Ser.*, vol. 12, no. 2, pp. 181–188, 1960.
- [38] G. Hurkx, "On the modelling of tunnelling currents in reverse-biased p - n junctions," *Solid-State Electron.*, vol. 32, no. 8, pp. 665–668, 1989.
- [39] G. A. M. Hurkx, D. B. M. Klaassen, and M. P. G. Knuvers, "A new recombination model for device simulation including tunneling," *IEEE Trans. Electron Devices*, vol. 39, no. 2, pp. 331–338, Feb. 1992.
- [40] N. Moulin, M. Amara, F. Mandorlo, and M. Lemiti, "Tunnel junction $I(V)$ characteristics: Review and a new model for p - n homojunctions," *J. Appl. Phys.*, vol. 126, Jul. 2019, Art. no. 033105.
- [41] M. Hermle, G. Létay, S. P. Philipps, and A. W. Bett, "Numerical simulation of tunnel diodes for multi-junction solar cells," *Prog. Photovolt.*, vol. 16, no. 5, pp. 409–418, Aug. 2008.
- [42] Setaurus Device User Guide, Version N-2017.09. Mountain View, CA, USA: Synopsys, Inc., Sep. 2017.
- [43] A. Gullino et al., "Physics-based modeling of AlGaAs tunnel junction VCSELs: A comparative appraisal," in *Proc. 23rd Int. Conf. Numer. Simul. Optoelectron. Devices*, 2023, pp. 99–100.
- [44] F. Bertazzi, M. Goano, G. Ghione, A. Tibaldi, P. Debernardi, and E. Bellotti, "Electron transport," in *Handbook of Optoelectronic Device Modeling and Simulation*, Boca Raton, FL, USA: CRC Press, 2017, ch. 2, pp. 35–80.
- [45] P.-F. Qiao, S. Mou, and S. L. Chuang, "Electronic band structures and optical properties of type-II superlattice photodetectors with interfacial effect," *Opt. Exp.*, vol. 20, no. 2, pp. 2319–2334, 2012.
- [46] G. Liu and S.-L. Chuang, "Modeling of sb-based type-II quantum cascade lasers," *Phys. Rev. B*, vol. 65, no. 16, 2002, Art. no. 165220.
- [47] I. Vurgaftman, J. R. Meyer, and L. R. Ram-Mohan, "Band parameters for III–V compound semiconductors and their alloys," *J. Appl. Phys.*, vol. 89, no. 11, pp. 5815–5875, Jun. 2001.
- [48] C. Rivas et al., "Full-band simulation of indirect phonon assisted tunneling in a silicon tunnel diode with delta-doped contacts," *Appl. Phys. Lett.*, vol. 78, no. 6, pp. 814–816, Feb. 2001.
- [49] M. Luisier and G. Klimeck, "Simulation of nanowire tunneling transistors: From the Wentzel–Kramers–Brillouin approximation to full-band phonon-assisted tunneling," *J. Appl. Phys.*, vol. 107, no. 8, Apr. 2010, Art. no. 084507.
- [50] M. Mohammed et al., "Phonon-assisted tunneling in direct-bandgap semiconductors," *J. Appl. Phys.*, vol. 125, no. 1, Jan. 2019, Art. no. 015701.

- [51] E. R. Hegblom, D. I. Babic, B. J. Thibeault, and L. A. Coldren, "Scattering losses from dielectric apertures in vertical-cavity lasers," *IEEE J. Select. Topics Quantum Electron.*, vol. 3, no. 2, pp. 379–389, Apr. 1997.
- [52] H. K. Bissessur, F. Koyama, and K. Iga, "Modeling of oxide-confined vertical-cavity surface-emitting lasers," *IEEE J. Select. Topics Quantum Electron.*, vol. 3, no. 2, pp. 344–352, Apr. 1997.
- [53] P. S. Wong, J. Yan, T. C. Wu, W. Kyi, J. Pao, and M. Riazat, "Tunnel junction 850-nm VCSEL for aperture uniformity and reliability," in *Proc. SPIE*, vol. 10122, pp. 72–76, 2017.
- [54] I. García, I. Rey-Stolle, and C. Algora, "Performance analysis of Al-GaAs/GaAs tunnel junctions for ultra-high concentration photovoltaics," *J. Phys. D*, vol. 45, no. 4, Jan. 2012, Art. no. 045101.
- [55] X. Gan et al., "GaAs tunnel junction grown using tellurium and magnesium as dopants by solid-state molecular beam epitaxy," *Japan. J. Appl. Phys.*, vol. 53, no. 2, Jan. 2014, Art. no. 021201.
- [56] M. Kamp, G. Mörsch, J. Gräber, and H. Lüth, "Te doping of GaAs using diethyl-tellurium," *J. Appl. Phys.*, vol. 76, no. 3, pp. 1974–1976, 1994.
- [57] H. C. Casey Jr. and M. B. Panish, *Heterostructure Lasers. Part A: Fundamental Principles*. New York, NY, USA: Academic Press, 1978.
- [58] P. Debernardi and G. P. Bava, "Coupled mode theory: A powerful tool for analyzing complex VCSELs and designing advanced devices features," *IEEE J. Select. Topics Quantum Electron.*, vol. 9, no. 3, pp. 905–917, May/Jun. 2003.
- [59] P. Debernardi, A. Kroner, F. Rinaldi, and R. Michalzic, "Surface relief versus standard VCSELs: A comparison between experimental and hot-cavity model results," *IEEE J. Select. Topics Quantum Electron.*, vol. 15, no. 3, pp. 828–837, May/Jun. 2009.
- [60] V. Torrelli, A. Tibaldi, F. Bertazzi, M. Goano, and P. Debernardi, "Modeling of single-mode high-power VCSEL arrays," in *Proc. 23rd Int. Conf. Numer. Simul. Optoelectron. Devices*, 2023, pp. 93–94.
- [61] A. E. Bond, P. D. Dapkus, and J. D. O'Brien, "Aperture placement effects in oxide-defined vertical-cavity surface-emitting lasers," *IEEE Photon. Technol. Lett.*, vol. 10, no. 10, pp. 1362–1364, Oct. 1998.
- [62] B. Demeulenaere, P. Bienstman, B. Dhoedt, and R. G. Baets, "Detailed study of AlAs-oxidized apertures in VCSEL cavities for optimized modal performance," *IEEE J. Quantum Electron.*, vol. 35, no. 3, pp. 358–367, Mar. 1999.
- [63] G. Almuneau et al., "Real-time in situ monitoring of wet thermal oxidation for precise confinement in VCSELs," *Semicond. Sci. Technol.*, vol. 23, no. 10, Sep. 2008, Art. no. 105021.
- [64] G. Lafleur, G. Almuneau, A. Arnoult, H. Camon, and S. Calvez, "Anisotropy in the wet thermal oxidation of AlGaAs: Influence of process parameters," *Opt. Mater. Exp.*, vol. 8, no. 7, pp. 1788–1795, Jul. 2018.
- [65] X. Yang, M. Li, G. Zhao, Y. Zhang, S. Freisem, and D. Deppe, "Oxide-free vertical-cavity surface-emitting lasers with low junction temperature and high drive level," *Electron. Lett.*, vol. 50, no. 20, pp. 1474–1475, 2014.
- [66] A. Pissis, U. Siegenthaler, D. Bonfrate, P. D. Kanungo, and E. Zibik, "940 nm high power single transverse mode coherent VCSEL array with tunnel junction lithographic aperture," in *Proc. 27th Int. Semicond. Laser Conf.*, 2021, pp. 1–2.